November 15, 1991

TDA Progress Report 42-107

Trajectory and Navigation System Design for Robotic and Piloted Missions to Mars

S. W. Thurman
Navigation Systems Section

S. E. Matousek
Mission Design Section

Future Mars exploration missions, both robotic and piloted, may utilize Earth-to-Mars transfer trajectories that are significantly different from one another, depending upon the type of mission being flown and the time period during which the flight takes place. The use of new or emerging technologies for future missions to Mars, such as aerobraking and nuclear rocket propulsion, may yield navigation requirements that are much more stringent than those of past robotic missions, and are very difficult to meet for some trajectories. This article explores the interdependencies between the properties of direct Earth-to-Mars trajectories and the Mars approach navigation accuracy that can be achieved using different radio metric data types, such as ranging measurements between an approaching spacecraft and Mars-orbiting relay satellites, or Earth-based measurements such as coherent Doppler and very long baseline interferometry. The trajectory characteristics affecting navigation performance are identified, and the variations in accuracy that might be experienced over the range of different Mars approach trajectories are discussed. The results predict that three-sigma periapsis altitude navigation uncertainties of 2 to 10 km can be achieved when a Mars-orbiting satellite is used as a navigation aid.

I. Introduction

The exploration of Mars to date has been accomplished by unmanned spacecraft using low-energy ballistic transfer trajectories to reach their destinations. NASA's ambitious plans for future Mars exploration call for a variety of robotic and piloted spacecraft to investigate the Red Planet from orbit and on its surface. These missions may employ new technologies, such as nuclear rocket propulsion, which make it possible to send large payloads to Mars along high-energy trajectories that are inaccessible to current chemically propelled launch-vehicle/upper-stage combinations. Another concept receiving serious consideration is aerobraking, in which a spacecraft executes a controlled

passage through the Martian atmosphere to decelerate into a closed orbit or to initiate a descent to the surface of the planet. Aerobraking can also be employed by a spacecraft already orbiting Mars to modify its orbit.

The successful use of aerobraking for orbit insertion (called aerocapture) or direct entry and landing may require approach navigation accuracies that are much more stringent than those typically needed to support a propulsive orbit insertion, depending upon the target orbit (or landing point) and the characteristics of the aerobrake vehicle itself. For example, previous studies of navigation requirements for Mars aerocapture have found that aerocapture vehicles of moderate maneuver capability (maximum lift-to-drag ratios of 0.5 to 0.7) must be delivered to within 5 to 20 km in altitude and 30 to 50 km along the flight path (downtrack) at the nominal atmospheric entry point, which typically occurs just prior to closest approach [1,2]. This is in contrast to an altitude delivery requirement at closest approach of about 300 km for the Mars Observer mission, which will perform a propulsive orbit insertion.[1] Spacecraft using high-thrust nuclear propulsion (nuclear-thermal rocket engines, in which a solid or gaseous core reactor is used to heat a working fluid such as hydrogen) will probably also require greater delivery accuracies than Mars-Observer–class missions, as they may possess Mars approach velocities of up to 10 km/sec [3]; in contrast, this figure will be about 2.5 km/sec for Mars Observer.

Several studies have analyzed the performance of different pre-aerocapture approach navigation schemes at Mars [1–2,4–6]. These studies, which have addressed a relatively small subset of possible Mars approach trajectories, investigated radio and optical data that provide direct measurements of the Mars-relative trajectory of an approaching spacecraft: spacecraft onboard optical imaging of Martian moons, ranging measurements between a Mars-orbiting communications relay satellite and the approaching spacecraft, and Earth-based dual-spacecraft radio interferometry, again using a Mars relay satellite in conjunction with the approaching spacecraft. This article describes a preliminary assessment of the impact of different approach trajectories, arising from different types of direct Earth–Mars transfer trajectories, on the performance of the radio navigation schemes involving a Mars relay satellite listed above, focusing on the performance needed to support the use of aerobraking. The guidance accuracy that can be achieved by modern robotic spacecraft is also investigated briefly to provide some indication of the relative importance of guidance errors versus orbit determination errors in Mars approach navigation system design.

[1] P. B. Esposito, *Mars Observer Navigation Plan*, JPL D-3820, Rev. C (internal document), Jet Propulsion Laboratory, Pasadena, California, June 5, 1990.

II. Direct Transfer Trajectories

There are many different trajectories that can be used to reach Mars from the Earth. Current launch vehicle capabilities limit the available trajectories to those with reasonable launch energies for spacecraft of modest (less than about 6000 kg) mass. Avoidance of excessive transit time generally limits the range of possible trajectories to those that take less than one full revolution around the Sun. After these initial constraints are taken into account, direct transfer trajectories known as type-1 (transfer angle between 0 and 180 deg) or type-2 (transfer angle between 180 and 360 deg) are left to consider. Transfers that involve a flyby of Venus after launch from Earth are also possible, but these trajectories are beyond the scope of this study [7].

A. Trajectory Characteristics

For a given launch opportunity, either a type-1 or a type-2 trajectory can be selected. Type-1 trajectories generally have shorter transit times than type-2 trajectories; however, in most cases type-1 trajectories also require a higher launch energy than type-2 trajectories for a given launch opportunity. Within the general categories of type-1 or -2 lie other trajectory options. One obvious choice is to optimize for a minimum launch energy (generally defined in terms of the parameter called C_3, with units of km^2/sec^2, or hyperbolic excess launch velocity, V_∞, which is equal to $\sqrt{C_3}$). Another alternative is to minimize the arrival velocity at Mars. Unfortunately, trajectories optimized for minimum launch energy have greater arrival velocities at Mars than trajectories optimized for minimum Mars arrival velocity. Conversely, trajectories optimized for minimum arrival velocity at Mars possess larger launch energies at Earth than trajectories optimized for minimum launch energy.

Figure 1 shows four possible trajectories for the 1998 launch opportunity. Each of these trajectories corresponds to a type-1 or type-2 transfer, further subdivided into a minimum launch energy case and a minimum arrival velocity case. While trajectories for different launch opportunities would, by necessity, differ somewhat from those shown in Fig. 1, the basic appearance of the different trajectory types relative to each other would not change significantly. Figure 2 depicts the Mars arrival geometry corresponding to the type-1 minimum launch energy trajectory, assuming

a polar circular target orbit with an altitude of 700 km. Figure 3 depicts the Mars arrival geometry for the type-2 minimum launch energy trajectory, assuming that the target orbit is the same as that in Fig. 2. In both Figs. 2 and 3, the frames showing the view from "above" the ecliptic plane represent how the trajectory would look when viewed from the ecliptic north pole looking south at the ecliptic plane, the mean plane of the Earth's orbit. Also in Figs. 2 and 3, note that the angle between the Earth–Mars radial line and the type-1 (Fig. 2) incoming trajectory is significantly different from the type-2 (Fig. 3) trajectory.

B. Trajectory Design Issues

There are many factors that can influence the selection of a particular Earth–Mars trajectory. However, it is possible to single out a few major constraints that affect trajectory selection and, consequently, Mars approach navigation performance. The first, and most obvious, constraint on a trajectory is that it must deliver a spacecraft to Mars. The energy imparted from the launch vehicle system (launch vehicle, upper stages, and any additional boost stages) to the spacecraft at injection must match the spacecraft velocity to the velocity required at a particular point in space to follow a given transfer trajectory. There are many different options for meeting this constraint [8, 9]. For robotic missions, the trajectory design process generally consists of evaluating trade-offs between minimizing the launch energy, and hence the injection velocity, and the Mars arrival velocity, subject to criteria derived from the mission objectives. For piloted missions, this process is further complicated by the additional constraint that a return leg is also needed, therefore the launch energy from Mars and the arrival velocity at Earth for a return trip must also be considered along with the corresponding parameters for the Earth–Mars trajectory (Soldner [5] describes the round-trip trajectory design problem for piloted missions).

Table 1 summarizes the range of launch energies and Mars arrival velocities for minimum launch energy and minimum arrival energy type-1 and type-2 trajectories, obtained from an analysis of Mars launch opportunities between 1995 and 2020. Nuclear-rocket-propelled spacecraft may be able to utilize fast "sprint" trajectories, which are type-1-class trajectories with larger launch energies and arrival velocities than the optimized trajectories given in Table 1.

The range of launch azimuths available from a particular launch site is another constraint that must be considered. The launch-azimuth constraints for the Kennedy Space Center (KSC) are shown in Fig. 4. Range safety considerations call for a launch trajectory over water for the early part of the flight (it should be noted that not all of the allowable azimuths shown in Fig. 4 are necessarily available because of islands in certain areas of the allowable envelope). From KSC, the available range of launch azimuths effectively restricts the injection asymptote declination (the inclination of the injection velocity vector relative to the Earth's equatorial plane) to the range from about −53 to +53 deg. This restriction can, in turn, make it very difficult to achieve the injection velocity vector required to utilize some direct Earth–Mars transfers for certain launch opportunities. For example, the type-1 minimum launch energy trajectory for the 2001 launch opportunity requires an injection asymptote declination of 54 deg, which is unreachable from KSC with current U. S. launch vehicles because of launch azimuth constraints. Even if the required injection asymptote declination can be reached, trajectories with large declination magnitudes generally require greater launch energies from a near-equatorial launch site such as KSC, effectively reducing the available payload mass for the mission. Other mission design considerations such as the length of the daily launch window, desired Mars arrival geometry, and target orbit influence the transfer trajectory design process as well [9].

III. Navigation Accuracy Analysis

The objective of approach-phase navigation is to deliver a spacecraft to a chosen aim point at a desired time. The navigation system for this task may consist of many different physical elements, located both on the spacecraft and on the Earth, but it must perform two primary functions, regardless of the means employed: orbit determination, which is the process of determining the current and predicted future flight path of a spacecraft, and guidance (maneuver analysis/design), which is the process of planning and executing trajectory correction maneuvers (TCMs) that will remove known deviations of the spacecraft from the intended flight path and will satisfy other mission constraints. The overall navigation, or delivery, accuracy achieved by the end-to-end navigation system depends on the accuracy to which both the orbit determination and guidance functions are performed.

A. Maneuver Analysis

Guidance for interplanetary spacecraft is normally carried out using propulsive maneuvers of short duration for flight path control (the exception being spacecraft employing low-thrust nuclear or solar-electric propulsion systems that may operate continuously for extended periods) to

achieve a desired close flyby of a target body or to decelerate into a closed orbit upon arrival. In this section, approximate estimates of the navigation uncertainty due to guidance errors are developed using propulsion-system performance data representative of modern robotic spacecraft. In subsequent sections, approximate orbit-determination accuracy estimates are developed and used along with the guidance-error estimates to compute statistics for the overall navigation altitude error at the vacuum periapsis point (closest approach).

Maneuver calculations are most often performed using an asymptotic, or "B-plane," coordinate system, defined in Fig. 5. The origin of this system is the center of mass of the target planet. The B-plane coordinates describing the trajectory are defined in terms of the orthogonal unit vectors $\hat{S}$, $\hat{T}$, and $\hat{R}$. $\hat{S}$ is parallel to the incoming asymptote of the approach hyperbola, while $\hat{T}$ usually lies in either the ecliptic plane or the equatorial plane of the target body; $\hat{R}$ completes the triad. The aim point is defined by $\vec{B}$, known as the "miss" vector, and the desired arrival time, which is expressed in terms of the linearized time of flight (LTOF), is defined as the time before closest approach, if it is assumed that the miss vector has zero magnitude. Both maneuver-execution errors and orbit-determination errors are normally characterized by a three-sigma B-plane dispersion ellipse, shown in Fig. 5, and the three-sigma uncertainty in linearized time of flight. In Fig. 5, SMAA is the semimajor axis of the dispersion ellipse, while SMIA is the semiminor axis of the dispersion ellipse.

During a mission, the miss vector and linearized time of flight corresponding to a spacecraft's actual trajectory are estimated repeatedly during the orbit-determination process and compared with their desired values. If the current estimated aim point is sufficiently removed from the desired aim point, then a TCM must be performed at some point to remove this deviation. The placement and design of TCMs must take into account a great many considerations; these have been described in much greater detail than can be given here by Hintz and Chadwick [10, 11].

For roughly the final 10 to 14 days before encounter, a spacecraft approaching Mars will have a nearly constant velocity with respect to the planet, directed along the Mars–spacecraft radial line, until it is within 12 to 24 hr of periapsis (closest approach) [8]. During this period, small changes in the B-plane coordinates resulting from a small, instantaneous spacecraft velocity change (an excellent approximation for most TCMs) vary roughly linearly with time. This relationship can be expressed as

$$\Delta\vec{B} = \mathbf{K}\Delta\vec{v} \tag{1}$$

where

$$\Delta\vec{B} = [\Delta B{\cdot}T,\ \Delta B{\cdot}R, \Delta LTOF]^T$$

$$\Delta\vec{v} = [\Delta v_T, \Delta v_R, \Delta v_S]^T$$

$$\mathbf{K} \approx \begin{bmatrix} t & 0 & 0 \\ 0 & t & 0 \\ 0 & 0 & t/V_\infty \end{bmatrix}$$

and

$\Delta B{\cdot}T, \Delta B{\cdot}R$ = changes in T and R components of $\vec{B}$, respectively

$\Delta LTOF$ = change in linearized time of flight

$\Delta v_T, \Delta v_R, \Delta v_S$ = T, R, and S velocity increments

t = time to go before closest approach

V_∞ = hyperbolic approach velocity

The approximation given for the $\mathbf{K}$ matrix in Eq. (1) effectively assumes that the target planet has no mass. It has been shown that for a small planet such as Mars, Eq. (1) is also a fairly good approximation (±20 percent) until roughly the final 12 to 24 hours of the approach phase [12].

In a typical robotic mission, a TCM to remove execution errors from earlier maneuvers will be scheduled at about 10 days prior to encounter. This point is near enough to encounter to effect fairly small changes in the aim point, but far enough out so that there is sufficient time to redetermine the orbit, and design and execute a final TCM at 1 to 2 days out, if necessary. The error covariance matrix for the B-plane coordinates prior to each maneuver is just the sum of the orbit-determination error covariance and the guidance-error covariance at the maneuver epoch, assuming that the orbit-determination errors and guidance errors are independent:

$$\mathbf{\Lambda}_{\Delta\vec{B}} = \mathbf{\Lambda}_{OD} + \mathbf{\Lambda}_G \tag{2}$$

where

$\mathbf{\Lambda}_{\Delta\vec{B}}$ = B-plane coordinate error covariance matrix

$\mathbf{\Lambda}_{OD}$ = B-plane coordinate orbit determination error covariance

Λ_G = B-plane coordinate guidance error covariance

The guidance-error covariance reflects the B-plane coordinate uncertainty obtained upon completion of the previous maneuver. Equation (1) can be inverted to compute a maneuver to correct for a known aim-point error, $\Delta\vec{B}$:

$$\Delta\vec{v} = \mathbf{K}^{-1}\Delta\hat{\vec{B}} \tag{3}$$

where

$\Delta\hat{\vec{B}}$ = orbit-determination estimate of $\Delta\vec{B}$ at maneuver epoch

Since the maneuver computed using Eq. (3) must by necessity be based on an estimate of $\Delta\vec{B}$, it becomes apparent that the accuracy of the maneuver will be limited by orbit-determination accuracy. Hence, it is desirable that maneuvers be executed only when the orbit-determination uncertainty at the maneuver epoch is small relative to the size of the guidance errors to be removed from the trajectory.

After a maneuver, the B-plane coordinate error covariance, assuming that the orbit-determination errors and maneuver-execution errors are independent, is

$$\Lambda_{\Delta\vec{B}} = \Lambda_{OD} + \mathbf{K}\Lambda_E\mathbf{K}^T \tag{4}$$

where

Λ_E = maneuver-execution error covariance

The B-plane coordinate covariance in Eq. (4) becomes the guidance-error covariance in Eq. (2) for the next maneuver. When a maneuver $\Delta\vec{v}$ is computed, the errors in the orbit-determination estimate of the trajectory at that time result in an erroneous computation; hence, orbit-determination errors are effectively translated into guidance errors as each successive maneuver is performed. Maneuver-execution errors, caused by imperfect execution of the planned maneuver, are typically broken into fixed errors and proportional errors, both in $\Delta\vec{v}$ magnitude and direction. Representative three-sigma values for large robotic spacecraft such as Galileo and Cassini are about 1.0 mm/sec fixed magnitude and direction, 5.0 percent proportional magnitude, and 10.0 mrad/axis proportional direction.

B. Guidance-Error Calculations

Using Eqs. (2), (3), and (4), approximate guidance (maneuver-execution error) dispersion ellipses can be calculated for TCMs performed near Mars. The results given below were computed for TCMs assumed to be located at 10 days (hereafter referred to as TCM1) and 1 day (hereafter referred to as TCM2) prior to encounter, respectively.

The B-plane coordinate error covariance prior to TCM1 must be specified to determine the expected magnitude of this maneuver. The guidance-error covariance at this point was assumed to be a spherical-error ellipsoid, with a radius equal to 150 km, which is the semimajor axis (one-sigma) of the predicted B-plane dispersion ellipse for Mars Observer before its final TCM, 10 days prior to orbit insertion.[2] It should be noted here that the linearized time-of-flight uncertainty actually represents the position uncertainty in the $\hat{S}$ direction divided by the hyperbolic approach velocity, V_∞; therefore, a spherical position uncertainty ellipse is easily converted into an appropriate B-plane coordinate covariance. The orbit-determination error covariance was also assumed to be spherical, with a radius (one-sigma) of 10 km. This figure is representative of anticipated Earth-based radio-only tracking performance about 10 years from now, and is based on the study performed by Konopliv and Wood [4].

To compute the magnitude statistics of TCM1, Eq. (3) must first be used to compute the $\Delta\vec{v}$ covariance at 10 days out, using the assumed B-plane coordinate covariance. From the $\Delta\vec{v}$ covariance, the expected value and standard deviation of the maneuver magnitude can be obtained from the Monte Carlo simulation data describing maneuver magnitude statistics presented by Bollman and Chadwick [13]. The expected magnitude of TCM1 was found to be 28 cm/sec, with a standard deviation of 12 cm/sec; the three-sigma magnitude is then 64 cm/sec. The largest three-sigma execution error component, using the three-sigma maneuver execution statistics given above, was found to be 3 cm/sec. This value was assumed to apply to all three components of TCM1, resulting in a post-TCM1, three-sigma, B-plane guidance dispersion ellipse that is circular, with a radius of about 26 km. The post-TCM1 guidance and orbit-determination B-plane dispersions (three-sigma) and the root-sum-square (RSS) navigation (orbit-determination errors plus guidance errors) three-sigma dispersion ellipse are shown in Fig. 6(a). The corresponding post-TCM1 total LTOF uncertainty (three-sigma) is equal to 40 km/V_∞.

[2] Op. cit.

To compute the execution-error statistics for TCM2, the same process described above for TCM1 was repeated, with one modification. It was assumed that the orbit-determination B-plane covariance prior to TCM2 was small relative to the guidance-error covariance, which is just the post-TCM1 error covariance. It will be shown in the next section that this is a good assumption when a Mars-orbiting relay satellite is available as a navigation aid. The expected magnitude and standard deviation of TCM2 were then a function only of the post-TCM1 B-plane covariance. The three-sigma TCM2 magnitude was found to be 55 cm/sec. The largest maneuver-execution error component was again assumed to apply to all three spatial components of the maneuver, to construct a conservative estimate of the execution error dispersions. The three-sigma B-plane guidance dispersion ellipse for TCM2 is shown in Fig. 6(b). The corresponding three-sigma LTOF uncertainty was about 2.4 km/V_∞. The calculation of the orbit-determination B-plane dispersions needed to compute statistics for the total post-TCM2 navigation error uncertainty is the subject of the next section.

C. Orbit-Determination Analysis

To effectively support the final TCM (TCM2) before encounter, the errors in the trajectory solution used to compute the maneuver must be small relative to the guidance errors to be corrected, as discussed above. The orbit-determination errors at the time of TCM2 must also be small enough that the navigation errors at encounter, which include TCM2 maneuver-execution errors as well as orbit-determination errors, will not exceed the allowable requirements. Thus, after the first approach phase TCM (TCM1) is performed at 10 days out as assumed in this analysis, the approach trajectory must be redetermined accurately within 9 days, to support TCM2.

The Mars approach orbit-determination accuracy that can be achieved with conventional Earth-based radio metric data is fundamentally limited by errors in knowledge of the geocentric position and velocity of Mars itself, until the motion of the approaching spacecraft becomes dominated by the Martian gravity field. This does not occur until the last few hours or days before closest approach, depending on the approach trajectory characteristics. A spacecraft already orbiting Mars, since it is closely tied to the planet gravitationally, can be used as a radio navigation aid for an approaching spacecraft in two different ways. Ranging measurements between the two spacecraft have been shown to be potentially capable of determining the Mars-relative position and velocity of the approaching spacecraft to within a few kilometers and centimeters/second, respectively, although there exist tracking geometries that may yield significantly degraded performance [1,4,7]. Simultaneous tracking of a Mars orbiter or lander and an approaching spacecraft using Earth-based delta very long baseline interferometry (ΔVLBI), when used in conjunction with conventional Doppler and ranging data, has also been shown to be capable of similar accuracies [5]. In this section, the orbit-determination accuracy that can be obtained from both of these techniques is illustrated using approximate calculations of B-plane dispersions for short data arcs acquired near Mars.

1. Spacecraft–Spacecraft Ranging. The tracking geometry for spacecraft–spacecraft ranging measurements is depicted in Fig. 7. It has been shown previously [6] that the range observable, ρ, can be written simply as

$$\rho = r\left[1 - (2/r)r_s \cos\,\delta\,\cos\,(\alpha_s - \alpha) + r_s^2/r^2\right]^{1/2} \quad (5)$$

where

r = distance from approach spacecraft to center of Mars

δ = spacecraft declination relative to satellite orbit plane

α = spacecraft right ascension in satellite orbit plane

r_s = relay-satellite orbital radius

α_s = relay-satellite true anomaly

It can be seen from Eq. (5) that the range observable will enable a complete determination of the time histories of the approach spacecraft spherical coordinates relative to the satellite orbit plane. The ephemeris (position and velocity) of the relay satellite generally must also be estimated along with the approach spacecraft trajectory. To investigate the orbit-determination performance of spacecraft–spacecraft ranging, statistics associated with a weighted least-squares estimate of the B-plane coordinates describing the approach trajectory can be readily computed from the partial derivatives of Eq. (5) with respect to the approach trajectory and the relay-satellite orbit, and the error covariance assumed for the ranging data.

To compute the B-plane statistics, each ranging measurement, designated z, is assumed to consist of the actual range value and a zero-mean additive noise, ν:

$$z = \rho + \nu \quad (6)$$

Small changes in a series of ranging measurements, $\Delta\vec{z}$, from range values computed using an a priori estimate of the approach trajectory, are related to small changes in the vector of estimated parameters, $\Delta\vec{x}$, from their a priori values through a linearized matrix equation:

$$\Delta\vec{z} = \mathbf{A}\Delta\vec{x} + \vec{v} \tag{7}$$

where

$$\mathbf{A} = \begin{bmatrix} \partial z_1/\partial \vec{x} \\ \partial z_2/\partial \vec{x} \\ \cdot \\ \cdot \\ \partial z_n/\partial \vec{x} \end{bmatrix}$$

For spacecraft–spacecraft ranging covariance analysis, the estimated parameters were the epoch B-plane parameters, the magnitude and orientation of the asymptotic approach velocity vector, the position and velocity of the relay satellite at epoch, and a range measurement bias and bias rate, for a total of 14 parameters, all of which are constants. The error covariance for a weighted least-squares estimate of $\vec{x}$, designated $\mathbf{\Lambda_x}$, is

$$\mathbf{\Lambda_x} = \left[\tilde{\mathbf{\Lambda}}_{\mathbf{x}}^{-1} + \mathbf{A}^T\mathbf{\Lambda}_{\nu}^{-1}\mathbf{A}\right]^{-1} \tag{8}$$

In Eq. (8), $\tilde{\mathbf{\Lambda}}_{\mathbf{x}}$ is the a priori error covariance for the estimated parameters, and $\mathbf{\Lambda}_{\nu}$ is the error covariance for the noise-induced range measurement errors.

The assumptions used in the "baseline" spacecraft–spacecraft ranging scenario are given in Table 2. As in the guidance error computations, the approach spacecraft was assumed to nominally move at a constant velocity relative to Mars, since this is a good approximation for the trajectory until very near encounter. The approach velocity, V_∞, was chosen to be a midrange value, given the arrival velocity ranges from Table 1. The declination of the incoming velocity vector, given in Table 2 to be 20 deg, is defined with respect to the satellite orbit plane. The $\hat{T}$ axis (see Fig. 5), is taken here to lie in the Martian equatorial plane; therefore, by setting θ equal to zero, the miss vector lies in the Martian equatorial plane as well. In Table 2, the parameter h_p is the periapsis altitude for the actual hyperbolic flight path, whose incoming asymptote is coincident with the constant velocity trajectory used for the analysis. This value of h_p is representative of aerobraking approach trajectories used in previous studies [1,2].

B-plane dispersion ellipses calculated using three different values of range acquisition distance, the distance from Mars at which ranging data are first acquired, and two different values of the approach trajectory declination are shown in Fig. 8. In all cases shown in Fig. 8, the data cutoff point was assumed to be 24 hr prior to closest approach, and it was further assumed that the relay satellite was always in view of the approach spacecraft, so that ranging data were acquired continuously. Since data are taken up until the time of TCM2, it is implicitly assumed that the orbit-determination and TCM2 computations are performed onboard the approach spacecraft. The three-sigma LTOF uncertainty in all cases was less than 0.03 sec (equivalent to 120 m). These cases represent the performance that might be obtained with two-way ranging data. The range acquisition distance that can be achieved, which is seen in Fig. 8 to have a significant impact on orbit-determination performance, will depend upon the antenna sizes and transmitter power available on the two spacecraft, and the link frequency as well. The largest acquisition distance used, 2 million km, is reached about 5.8 days before encounter, while the minimum distance, 1 million km, is reached only 2.9 days from encounter.

In this analysis, the range measurement accuracy was assumed to vary linearly with the range between the two spacecraft (see Table 2); this behavior was found to be representative of a power-limited spacecraft–spacecraft ranging system in an earlier investigation [1]. It should be remembered that the relay-satellite ephemeris was estimated along with the trajectory of the approach spacecraft. The relay-satellite a priori position and velocity uncertainties given in Table 2 are representative of the level of accuracy that can typically be achieved using Earth-based Doppler tracking data. Since it takes time to estimate the relay-satellite ephemeris from the ranging data, along with the other estimated parameters, changes in the a priori relay-satellite covariance will affect the accuracy achieved for the approach spacecraft, especially in cases when the range acquisition distance is small and the data arc is thereby short in length.

In Fig. 8, note than the B-plane dispersion ellipses for the small declination cases, Fig. 8(b), are much larger than those for the corresponding cases in which baseline declination from Table 2 was used, Fig. 8(a). When the magnitude of the declination angle (δ) is small, range measurements are relatively insensitive to small changes in

declination, which in Fig. 8 corresponds roughly to the $\hat{R}$ direction. This behavior can be illustrated by taking the partial derivative of Eq. (5) with respect to δ, which to first order is the sensitivity of range to a small change in δ. If it is assumed that $r_s/r \ll 1$ (a good assumption until the last one or two days before closest approach), this partial derivative is approximately

$$\partial\rho/\partial\delta \sim r_s \sin\delta \cos(\alpha_s - \alpha) \tag{9}$$

From Eq. (9), it is apparent that when δ is small, it will be difficult to accurately determine the declination angle (and hence its rate of change as well) from ranging data.

2. Earth-Based Doppler and Dual-Spacecraft Interferometry. Earth-based VLBI tracking of a Mars orbiter or lander and a spacecraft approaching Mars provides a direct measure of the Mars-relative approach trajectory, without requiring any communication between the two spacecraft. A detailed description of the dual-spacecraft VLBI measurement technique and the error sources affecting this data type is given by Edwards, Folkner, Border, and Wood [5]. Two-way (coherent) Doppler tracking of the approach spacecraft can to some degree sense the Mars-relative spacecraft trajectory, but only when the spacecraft is within the gravitational influence of Mars, which does not occur until the last few hours or days prior to closest approach. Since Doppler data sense the spacecraft motion along the Earth–spacecraft line of sight, and VLBI data sense primarily the motion perpendicular to the line of sight, these two data types provide complementary information when used together.

The information content of Doppler data acquired during the planetary approach phase has been described by Bollman [14]. A dual-spacecraft VLBI observation, illustrated in Fig. 9, consists of the time delay of radio signals observed by two stations; the radio signals from one spacecraft are differenced with the time delay from the other spacecraft as observed by the same two stations. As mentioned earlier, the trajectory of a Mars orbiter or lander with respect to Mars can be accurately determined from Earth-based tracking data, since it is gravitationally (or physically in the case of a lander) tied to Mars. Assuming the position of one of the two spacecraft is well known with respect to Mars, the dual-spacecraft VLBI observable, $\Delta\tau$, is approximately

$$\Delta\tau \approx \frac{\vec{r}_B}{c} \cdot (\vec{r} - \vec{r}_p) \tag{10}$$

where

$\vec{r}_B$ = baseline vector between the two participating stations

$\vec{r}$ = unit vector pointing toward approach spacecraft

$\vec{r}_p$ = unit vector pointing toward Mars

c = speed of light

During roughly the final two weeks before encounter, Eq. (10) becomes very nearly a function of the Mars-relative spacecraft position and the Earth baseline only:

$$\Delta\tau \approx \left(\frac{1}{c}\right) \frac{\vec{r}_B}{r} \cdot \vec{R}_{s/p} \tag{11}$$

where

$\vec{R}_{s/p}$ = approach spacecraft position with respect to Mars

r = approach spacecraft distance from Earth

From Eq. (11), it can be seen that the precision of the dual-spacecraft VLBI observable is directly proportional to the length of the baseline and inversely proportional to the Earth–spacecraft distance.

The assumptions used for calculating Doppler/dual-spacecraft VLBI orbit determination performance are given in Table 3. The trajectory parameters used (V_∞, θ, h_p) were the same as those for the spacecraft–spacecraft ranging cases (see Table 2). The estimated parameters were the B-plane coordinates and the arrival velocity vector components, a total of six in all. Calculations were performed for viewing geometries corresponding to two different Mars approach trajectories, representing type-1 and type-2 minimum launch energy transfers for the 1998 launch opportunity, respectively. The encounter geometries for these two cases are those shown in Figs. 2 and 3. The Mars relay-satellite used for acquiring dual-spacecraft VLBI data was assumed to have an ephemeris uncertainty of 2.0 km (one-sigma, each component), which was treated as a random error affecting the data. In Table 3, the dual-spacecraft VLBI measurement uncertainties are given in units of distance (cm) instead of units of time, since the observable, Eq. (10), can be viewed as a measure of distance simply by removing the factor $1/c$. The measurement accuracy assumed for the dual-spacecraft VLBI data was that given by Edwards for observations made at X-band (8.4-GHz) frequencies [5]. Since Earth-based data would likely be processed on Earth, the data cutoff point

was assumed to be 36 hr from encounter, allowing 12 hr for the ground processing needed for orbit determination and computation of the TCM2 maneuver at 24 hr from encounter.

B-plane and LTOF dispersions for three different dual-spacecraft VLBI data sets are shown in Fig. 10. The performance in the "baseline" cases, which include dual-spacecraft VLBI data acquired from two baselines formed by the DSN complexes near Goldstone, California; Madrid, Spain; and Canberra, Australia, is seen to be significantly better than that obtained when only one of the two DSN baselines is used. These results raise the question of whether spacecraft near Mars can be viewed from both the DSN Goldstone–Canberra and Goldstone–Madrid baselines for all possible Mars encounter dates. Figure 11 illustrates the overlap regions in which different portions of the celestial sphere can be viewed simultaneously from different pairs of DSN complexes. In Fig. 11, spacecraft declination is referred to the Earth's equatorial plane. Mars encounter declinations range from about −25.5 deg to +25.5 deg; for low-declination encounters, it can be seen from Fig. 11 that the Goldstone–Madrid baseline may not be able to view Mars and its vicinity. In fact, minimum elevation restrictions limit the lowest declination angle that can be effectively observed simultaneously by Goldstone and Madrid to about −20 deg.

D. Total Periapsis Altitude Navigation Error

This section presents the three-sigma periapsis altitude uncertainties that could be obtained using the hypothetical guidance and orbit-determination scenarios developed in the previous sections. The statistics of the altitude error at periapsis can be readily calculated from the total navigation B-plane error covariance, consisting of orbit-determination and guidance-error statistics, at completion of the final trajectory correction maneuver. As stated in the Introduction, the periapsis altitude error that can be tolerated by aerobrake vehicles possessing moderate (0.5 to 0.7) lift-to-drag ratios is between 5 and 20 km, depending upon the target orbit; this requirement is much more stringent than the periapsis downtrack error requirement (30 to 50 km) for these vehicles, and will therefore be the focus of the remaining discussion.

The magnitude of the miss vector, $|\vec{B}|$, is related to the periapsis radius, r_p, through the following formula from two-body orbital mechanics:

$$|\vec{B}| = r_p\sqrt{1+(2\mu)/(r_pV_\infty^2)} \qquad (12)$$

In Eq. (12), μ is the gravitational parameter of the target body. To first order, small errors in r_p due to errors in $|\vec{B}|$ can be expressed through the partial derivative of Eq. (12), yielding

$$\Delta r_p \approx \frac{|\vec{B}|}{r_p+(\mu/V_\infty^2)}\,\Delta|\vec{B}| \qquad (13)$$

From Fig. 6(b), the three-sigma uncertainty in $\vec{B}$ due to maneuver execution errors in the final TCM is about 2.4 km. For a nominal periapsis altitude of 20 km (r_p = 3417 km), this results in a three-sigma altitude uncertainty ranging from 1.95 km for an arrival velocity of 3.0 km/sec to 2.39 km for an arrival velocity of 10.0 km/sec. This guidance component of the altitude error represents the lower bound for the total navigation error. In looking at the orbit determination B-plane dispersions in Figs. 8 and 10, it can be seen that in most cases the guidance errors are small relative to the orbit-determination errors.

The previous section showed that the orbit-determination performance of spacecraft–spacecraft ranging varies with the declination of the approach trajectory with respect to the relay-satellite orbit plane and the maximum distance over which ranging data can be acquired. To investigate the sensitivity of the total altitude navigation error at periapsis to changes in V_∞ using spacecraft–spacecraft ranging for orbit determination, three-sigma altitude uncertainties were calculated over a range of V_∞ values for two different values of acquisition range. The error modeling assumptions used were those given in Table 2. The results are shown in Fig. 12; the minimum value of altitude uncertainty is about 2 km, which is primarily due to the guidance error component of the total navigation error. The calculations were repeated for circular orbits of different altitudes, ranging from 17,000 km (24.6-hr period, shown in Fig. 12) down to 5000 km (6.2-hr period). The results for the lower altitude orbits were not significantly different from those given in Fig. 12, and were therefore not shown, although this may not be the case for elliptic orbits [4]. In general, the data in Fig. 12 indicate that relatively large acquisition ranges may be needed to meet aerocapture approach navigation requirements for higher energy approach trajectories.

The navigation performance obtained when Earth-based Doppler and dual-spacecraft VLBI data are used for orbit determination may also vary with the Mars arrival velocity. The variation in periapsis altitude uncertainty with V_∞ for this case is shown in Fig. 13, for both the 1998 type-1 and type-2 trajectory geometries used previously (the error modeling assumptions used were those

given in Table 3). The curve for the type-2 trajectory in Fig. 13 ends at V_∞ = 6 km/sec since this was found to be roughly the upper bound for type-2 trajectories (see Table 1). The curve for the type-1 trajectory extends to V_∞ = 10 km/sec since the high-energy trajectories that might be followed by spacecraft utilizing nuclear rocket propulsion would be type-1-class trajectories. The behavior seen in Fig. 13 indicates that the impact of large values in this case is much less severe than that for spacecraft–spacecraft ranging. This is due to the fact that for the Earth-based data set, the length of the data arc is 8.5 days, regardless of the value of V_∞, whereas in the spacecraft–spacecraft ranging cases, the acquisition range constraint effectively reduces the length of the ranging data arc as V_∞ increases. Overall, though, the results in both Figs. 12 and 13 suggest that 2- to 10-km-altitude delivery accuracies can be achieved over a wide range of arrival velocities and viewing geometries using conventional impulsive guidance methods coupled with either spacecraft–spacecraft ranging or Earth-based dual-spacecraft VLBI.

The final sensitivity analysis investigated the impact of the Doppler data accuracy on the navigation performance that uses Earth-based Doppler and dual-spacecraft VLBI data. Figure 14 shows the variation in periapsis altitude navigation uncertainty with the Doppler data weight (accuracy) for the Doppler/dual-spacecraft VLBI baseline scenarios described in Table 3. The value of V_∞ used for all calculations shown in Fig. 14 was 4.0 km/sec. The Doppler accuracy used in the original baseline scenarios, 1.0 mm/sec, is representative of the performance of the current DSN Doppler system at S-band (2.3 GHz). At X-band (8.4 GHz), DSN Doppler accuracy is about 0.1 mm/sec, except for Sun–Earth–spacecraft angles of less than roughly 10 deg. In Fig. 14, the guidance error causes the altitude uncertainty curve to be essentially flat for Doppler weights of 0.1 mm/sec or better, while at the other extreme, once the Doppler weight reaches about 5.0 mm/sec, the altitude uncertainty curve becomes flat once again, indicating that the Doppler data are no longer affecting the altitude estimate. However, it appears that increasing the Doppler data accuracy from 1.0 mm/sec to 0.1 mm/sec may yield a significant improvement in performance, although it must be noted here that systematic error sources known to affect Doppler data, but not explicitly modeled in this analysis, may cause this improvement to be much less than that shown in Fig. 14 for the ideal case.

IV. Conclusions

Before stating any specific conclusions, it must be emphasized that the results of this analysis are products of the assumptions and error models used. Although the assumptions made for such parameters as maneuver-execution error statistics and data accuracies were, intentionally, conservative, the error models used to predict orbit-determination performance were relatively simple and did not include all error sources that may be present in actuality, but only those considered most significant. Previous experience with the kinds of approximations and assumptions used in this study suggest that the navigation-error statistics derived from these scenarios could be in error by as much as 20 percent, compared with results obtained with more complete error models.

Radio metric data types using a Mars-orbiting spacecraft as a navigation aid were found to be capable of delivering three-sigma periapsis altitude navigation errors of 2 to 10 km over a fairly wide range of Mars arrival velocities and viewing geometries. This level of performance equals or nearly meets that needed to support aerobraking for Mars orbit insertion by aerobrake vehicles possessing moderate lift-to-drag ratios. In most cases, the guidance-error contribution to the total navigation-error uncertainty was small relative to the orbit-determination errors. For spacecraft–spacecraft ranging data acquired from a Mars relay satellite, the orbit-determination performance was found to be sensitive to changes in the Mars arrival velocity, the declination of the approach trajectory with respect to the satellite orbit plane, and the maximum distance over which ranging data can be acquired.

The orbit-determination accuracy obtained from Earth-based Doppler/dual-spacecraft VLBI data sets was comparable to that obtained from spacecraft–spacecraft ranging data when two DSN baselines are used for obtaining dual-spacecraft VLBI data, but was much poorer when only one baseline was used. In addition, it was found that Doppler/dual-spacecraft VLBI performance was much less sensitive to changes in the Mars arrival velocity than that of spacecraft–spacecraft ranging data. Because of visibility restrictions for the DSN Goldstone–Madrid baseline, it may not be possible to obtain dual-spacecraft VLBI data from both of the currently available DSN baselines (Goldstone–Madrid and Goldstone–Canberra) for Mars encounter declinations (relative to the Earth's equator) less than about −20 deg.

References

[1] K. M. Spratlin, ed., *1989 Lunar/Mars Initiative Guidance, Navigation and Control Final Report*, CSDL-P-2838, The Charles Stark Draper Laboratory, Inc., Cambridge, Massachusetts, February 1990.

[2] S. W. Shepperd, D. P. Fuhry, and T. J. Brand, "Onboard Preaerocapture Navigation Performance at Mars," paper AAS 91-119, AAS/AIAA Spaceflight Mechanics Meeting, Houston, Texas, February 11–13, 1991.

[3] J. K. Soldner, "Round-Trip Mars Trajectories: New Variations on Classic Mission Profiles," paper AIAA-90-2932, AIAA/AAS Astrodynamics Conference, Portland, Oregon, August 20–22, 1990.

[4] A. K. Konopliv and L. J. Wood, "High-Accuracy Mars Approach Navigation with Radio Metric and Optical Data," paper AIAA-90-2907, AIAA/AAS Astrodynamics Conference, Portland, Oregon, August 20–22, 1990.

[5] C. D. Edwards, W. M. Folkner, J. S. Border, and L. J. Wood, "Spacecraft–Spacecraft Interferometry for Planetary Approach Navigation," paper AAS 91-181, AAS/AIAA Spaceflight Mechanics Meeting, Houston, Texas, February 11–13, 1991.

[6] S. W. Thurman and J. A. Estefan, "Mars Approach Navigation Using Doppler and Range Measurements to Surface Beacons and Orbiting Spacecraft," paper AAS 91-118, AAS/AIAA Spaceflight Mechanics Meeting, Houston, Texas, February 11–13, 1991.

[7] A. C. Young, J. A. Mulqueen, and J. E. Skinner, *Mars Exploration, Venus Swingby and Conjunction Class Mission Modes, Time Period 2000 to 2045*, NASA Technical Memorandum 86477, George C. Marshall Space Flight Center, Huntsville, Alabama, August 31, 1984.

[8] V. A. Lee and S. W. Wilson, "A Survey of Ballistic Mars-Mission Profiles," *J. Spacecraft Rockets*, vol. 4, no. 2, pp. 129–142, February 1967.

[9] A. B. Sergeyevsky, G. C. Snyder, and R. A. Cunniff, *Interplanetary Mission Design Handbook*, vol. 1, part 2, JPL Publication 82-43, Jet Propulsion Laboratory, Pasadena, California, September 15, 1983.

[10] G. R. Hintz, "An Interplanetary Targeting and Orbit Insertion Maneuver Design Technique," *J. Guidance Control*, vol. 5, no. 2, pp. 210–217, March–April 1982.

[11] G. R. Hintz and C. Chadwick, "Design and Analysis Techniques for Trajectory Correction Maneuvers," paper AIAA-84-2014, AIAA/AAS Astrodynamics Conference, Seattle, Washington, August 20–22, 1984.

[12] W. E. Bollman and M. G. Wilson, "Planetary Trajectory Correction Maneuver Dynamics on Approach Hyperbolic Trajectories," paper AIAA-86-2117, AIAA/AAS Astrodynamics Conference, Williamsburg, Virginia, August 18–21, 1986.

[13] W. E. Bollman and C. Chadwick, "Statistics of ΔV Magnitude for a Trajectory Correction Maneuver Containing Deterministic and Random Components," paper AIAA-82-1429, AIAA/AAS Astrodynamics Conference, San Diego, California, August 9–11, 1982.

[14] W. E. Bollman, "An Approximate Solution to the Analytical Partials of the Spacecraft's Geocentric Range-Rate During the Pre-Encounter Phase of a Planetary Mission," *JPL Space Programs Summary 37-52*, vol. 2, pp. 34–37, May–June 1968.

Table 1. Launch energy and Mars arrival velocity ranges (optimized Earth–Mars direct transfers, 1995–2020)

Trajectory type	Launch energy, km^2/sec^2		Arrival velocity, km/sec	
	Avg.	Range	Avg.	Range
Minimum launch energy (type-1)	12.2	8.0–19.0	4.1	2.7–6.0
Minimum launch energy (type-2)	10.9	8.0–17.0	3.6	2.5–6.0
Minimum arrival velocity (type-1)	20.0	8.0–31.0	3.6	2.3–4.0
Minimum arrival velocity (type-2)	16.6	9.0–31.0	2.9	2.4–4.0

Table 2. Spacecraft–spacecraft ranging baseline scenario

Approach spacecraft trajectory:
$V_\infty = 4.0$ km/sec, $\delta = 20.0$ deg, $\theta = 0.0$ deg, $h_p = 20.0$ km

Relay-satellite orbit:
Period = 24.62 hr (Mars-synchronous), altitude = 17,030.6 km

Ranging measurement accuracy, sample rate:
$\sigma_\rho = \rho/22,000$ (m), sample rate = 6 points/hr

A priori approach spacecraft uncertainties (one-sigma):
$\Delta\vec{B}\cdot\hat{T}, \Delta\vec{B}\cdot\hat{T} = 15.0$ km, $\Delta LTOF = 3.57$ sec, $\Delta V_\infty = 2.0$ cm/sec (each component)

A priori relay-satellite uncertainties (one-sigma):
Position = 2.0 km, velocity = 1.0 cm/sec (each component)

A priori ranging system uncertainties (one-sigma):
Range bias = 33.3 nsec (10.0 m), bias drift = 1.0×10^{-11} sec/sec (3.0 mm/sec)

Table 3. Earth-based Doppler/dual-spacecraft VLBI baseline scenarios

Type-1 minimum launch energy	Type-2 minimum launch energy
$r = 1.5 \times 10^8$ km	$r = 2.8 \times 10^8$ km
$\delta = -16.6$ deg[a]	$\delta = -14.4$ deg[a]
$\sigma_{VLBI} = 8.0$ cm	$\sigma_{VLBI} = 5.0$ cm
$\sigma_{Dop} = 1.0$ mm/sec	$\sigma_{Dop} = 1.0$ mm/sec

A priori approach spacecraft uncertainties (one-sigma):
$\Delta\vec{B}\cdot\hat{T}, \Delta\vec{B}\cdot\hat{T} = 15.0$ km, $\Delta LTOF = 3.75$ sec, $\Delta V_\infty = 2.0$ cm/sec (each component)

Doppler data schedule:
Continuous data (sample rate = 1 point/min) from E −10 days to E −1.5 days

Dual-spacecraft VLBI data schedule:
1 point/day each from DSN Goldstone–Madrid and Goldstone–Canberra baselines from E −10 days to E −1.5 days
(9 points/baseline, 18 points total)

[a] With respect to Earth's equatorial plane.

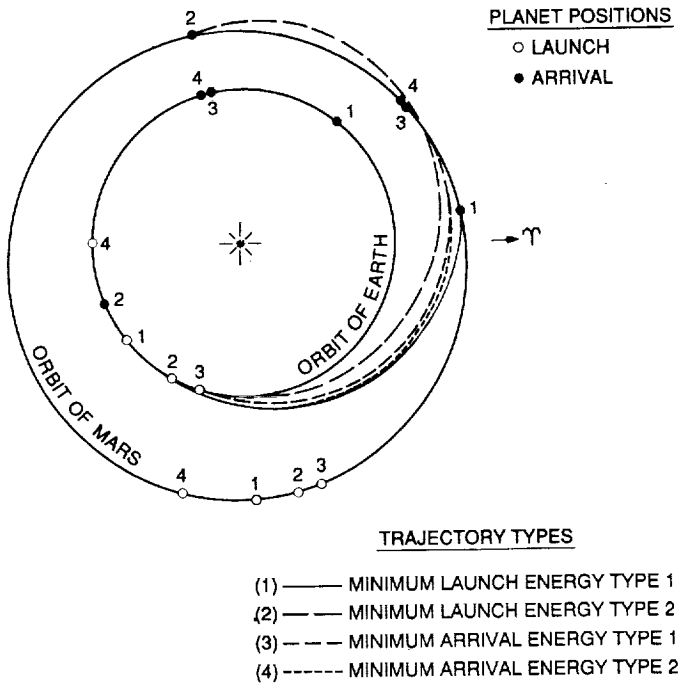

Fig. 1. Direct Earth–Mars transfer trajectories, 1998 launch opportunity.

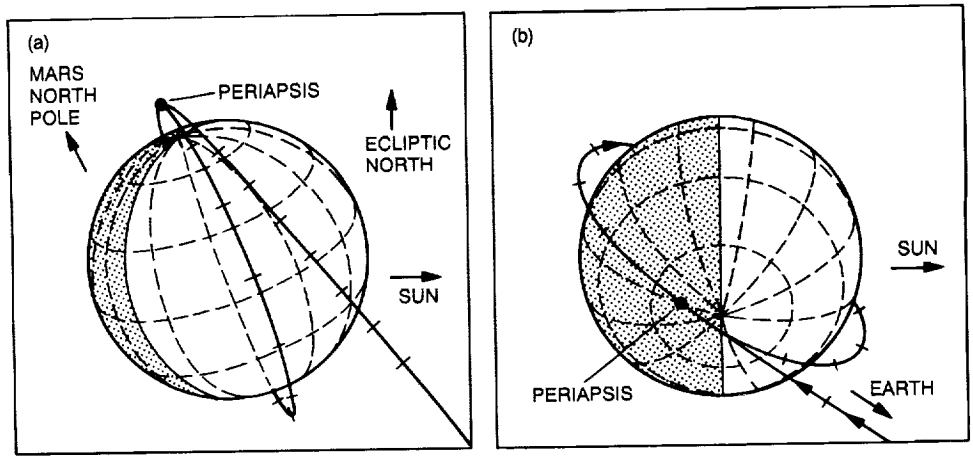

Fig. 2. Mars arrival geometry for type-1 transfer (1998 opportunity, minimum launch energy): (a) view from Earth, and (b) view from above ecliptic plane.

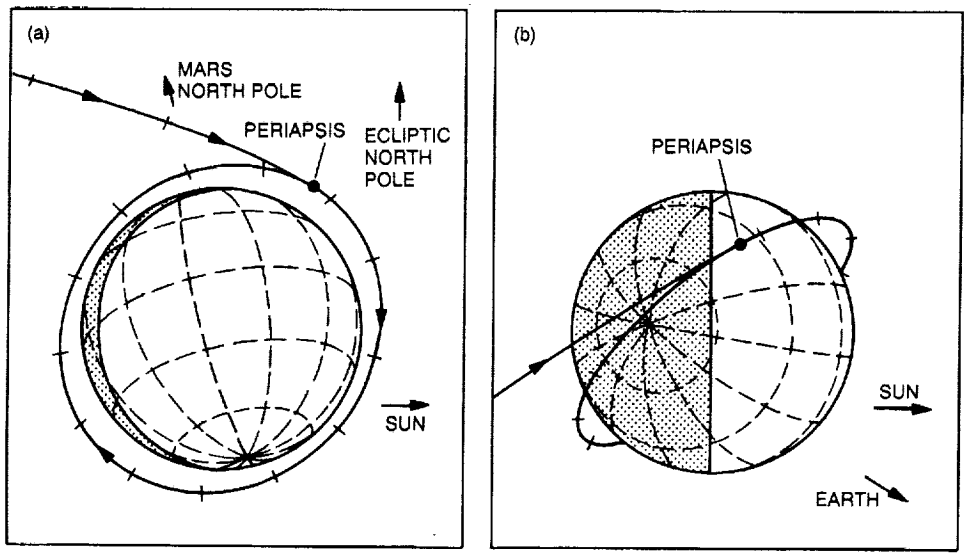

Fig. 3. Mars arrival geometry for type-2 transfer (1998 opportunity, minimum launch energy): (a) view from Earth, and (b) view from above ecliptic plane.

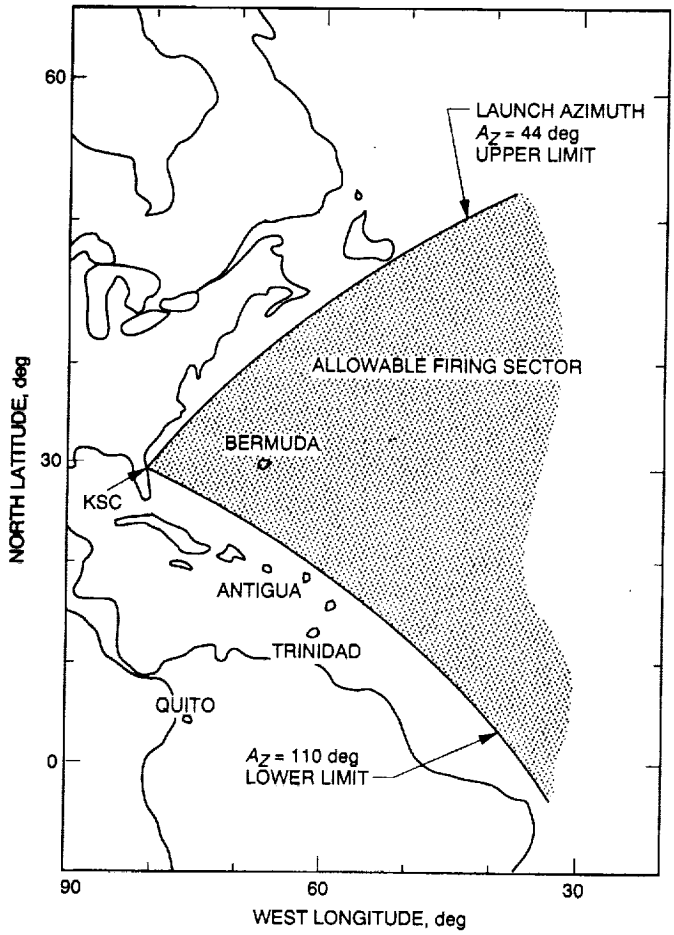

Fig. 4. Launch azimuth constraints for Kennedy Space Center.

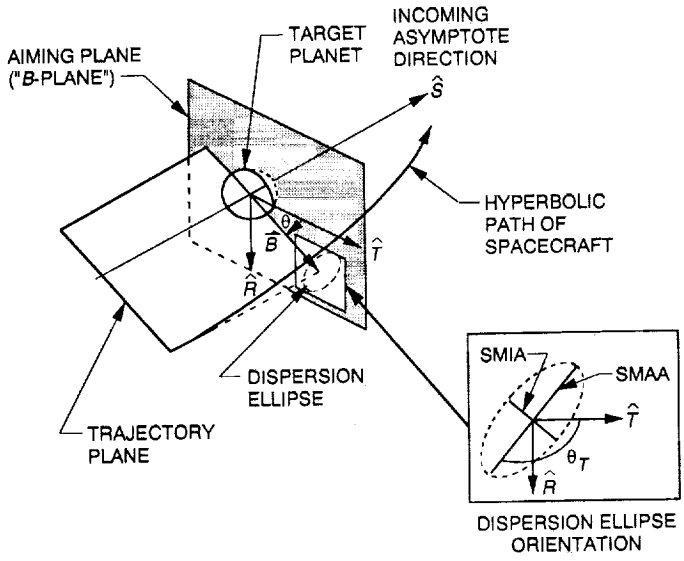

Fig. 5. Asymptotic coordinate system definition.

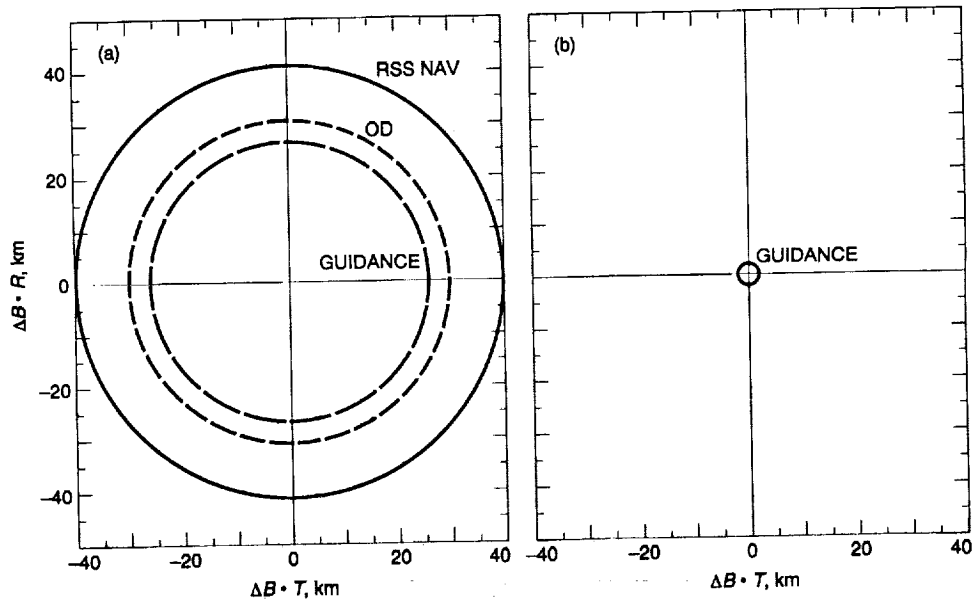

Fig. 6. Post-TCM1 and -TCM2 three-sigma *B*-plane dispersions: (a) post-TCM1, and (b) post-TCM2.

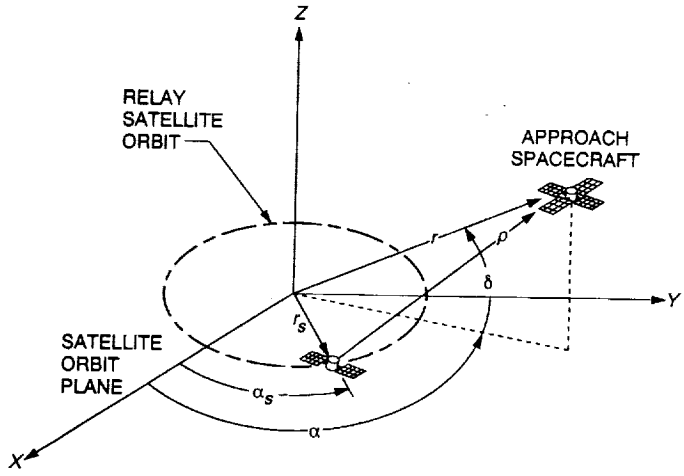

Fig. 7. Spacecraft–spacecraft tracking geometry.

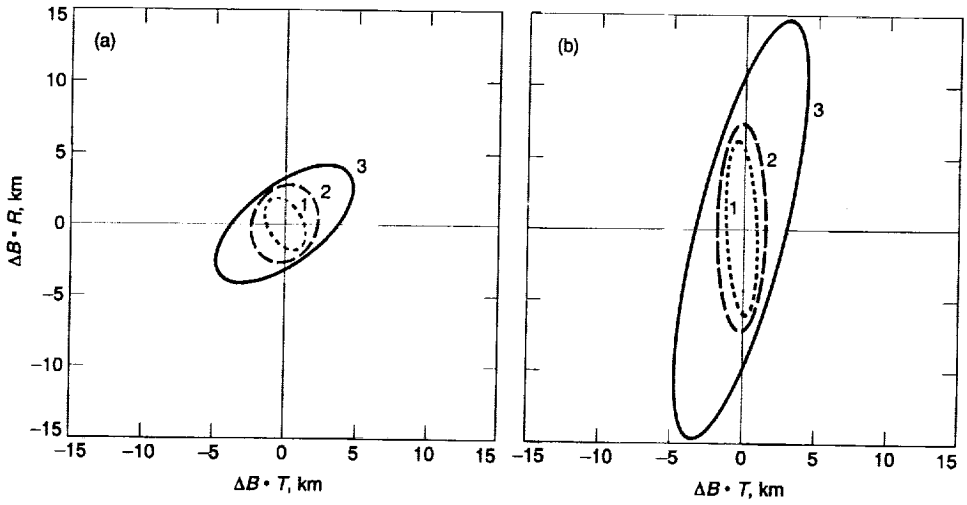

1. ACQUISITION RANGE = 2.0×10^6 km
2. ACQUISITION RANGE = 1.5×10^6 km
3. ACQUISITION RANGE = 1.0×10^6 km

Fig. 8. Three-sigma *B*-plane dispersions for spacecraft–spacecraft ranging cases (24-hr data cutoff): (a) δ = 20 deg, and (b) δ= 5 deg.

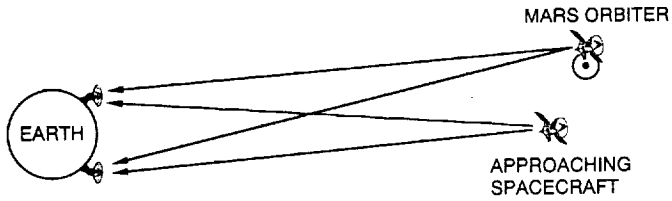

Fig. 9. Dual-spacecraft VLBI observation.

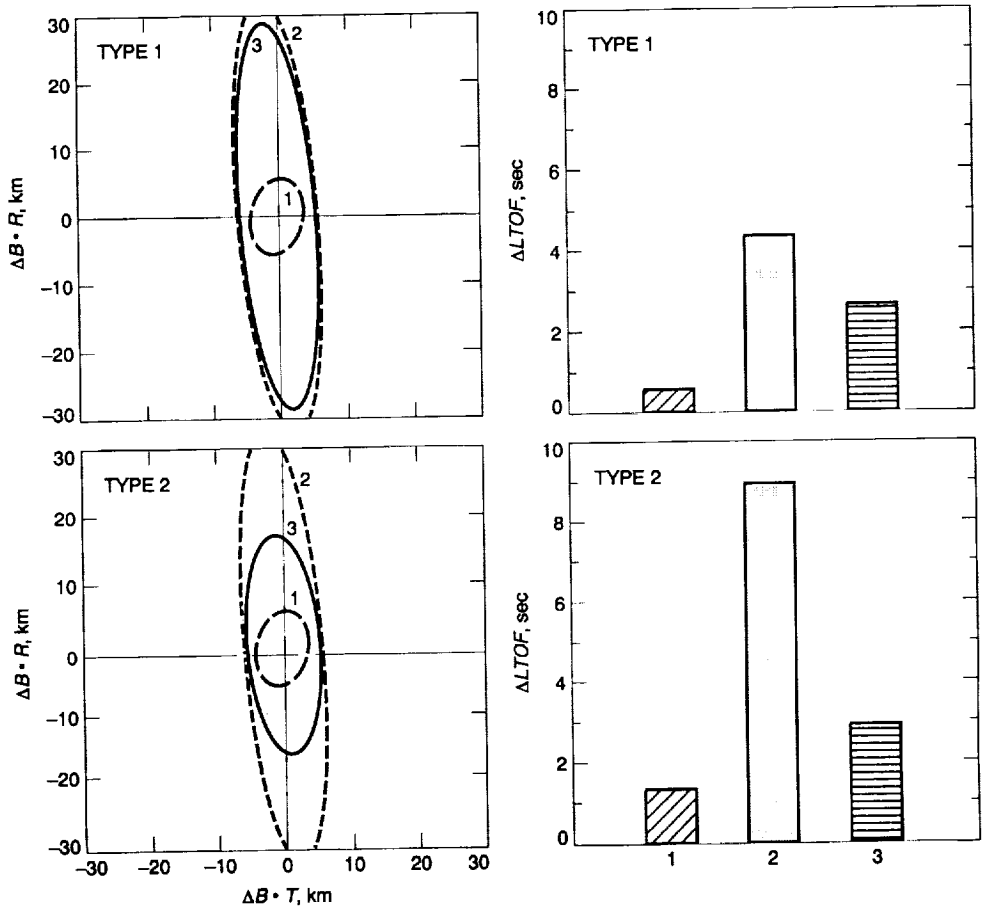

1. VLBI DATA FROM TWO BASELINES
2. VLBI DATA FROM GOLDSTONE-CANBERRA ONLY
3. VLBI DATA FROM GOLDSTONE-MADRID ONLY

Fig. 10. Three-sigma *B*-plane dispersions and LTOF uncertainty for Earth-based Doppler/dual-spacecraft VLBI cases (36-hr data cutoff).

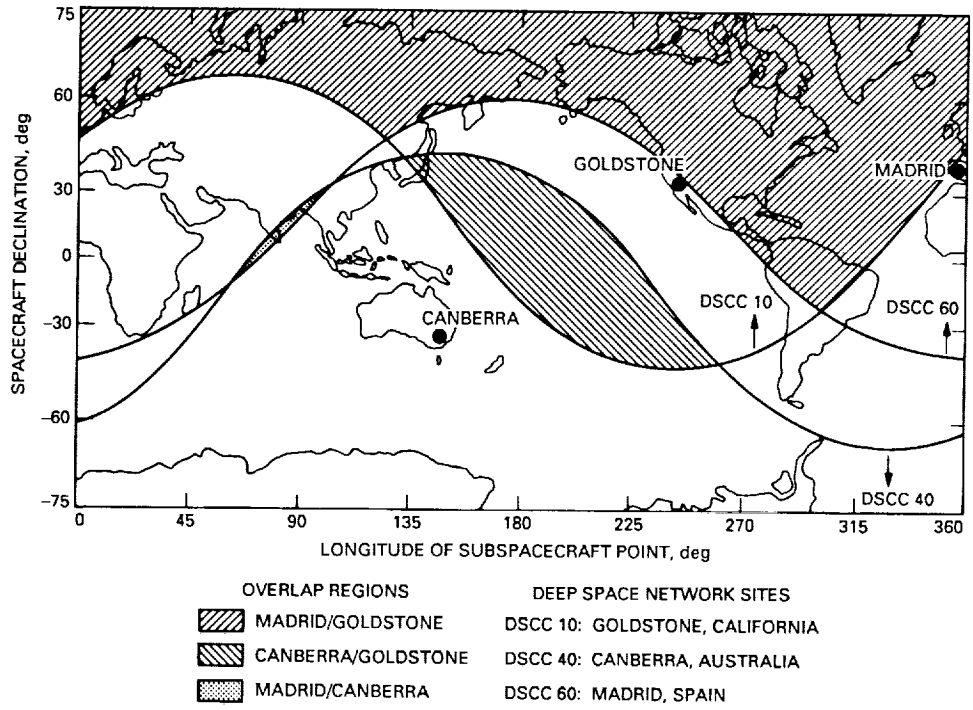

Fig. 11. Deep Space Network intercontinental baseline visibility regions.

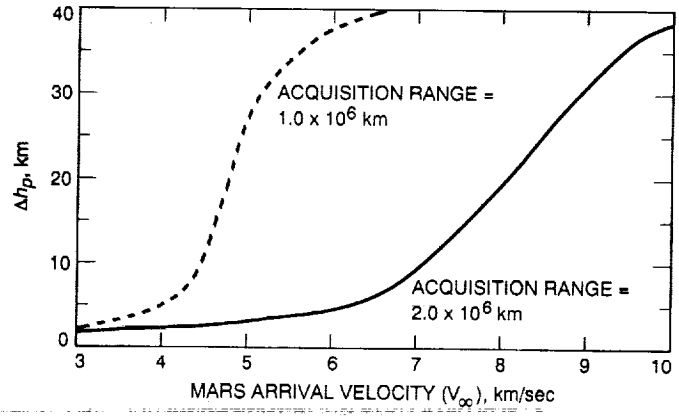

Fig. 12. Three-sigma altitude uncertainty versus Mars arrival velocity (spacecraft–spacecraft ranging).

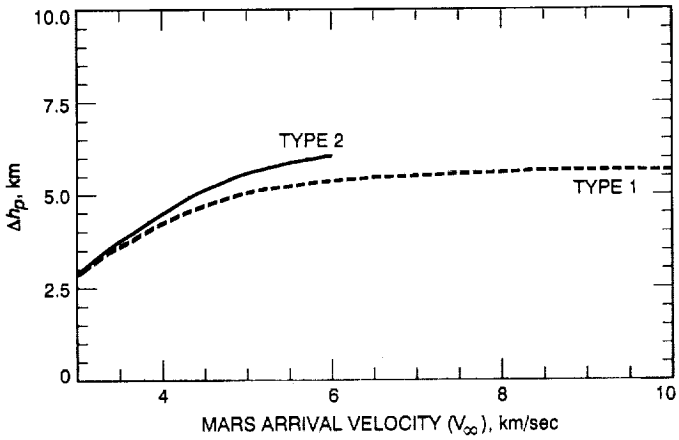

Fig. 13. Three-sigma altitude uncertainty versus Mars arrival velocity (DSN Doppler/dual-spacecraft VLBI).

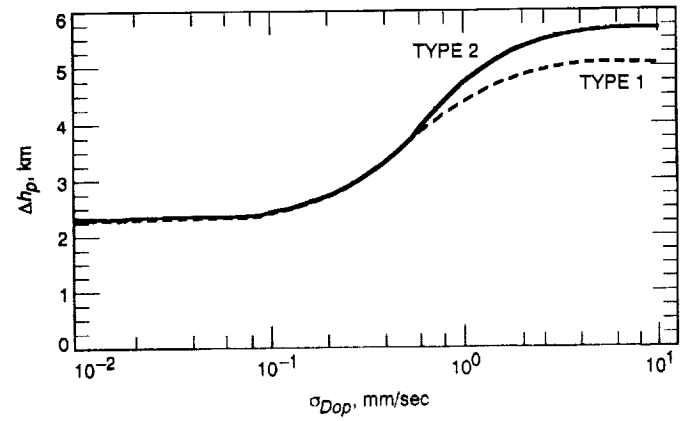

Fig. 14. Three-sigma altitude uncertainty versus Doppler weight (DSN Doppler/dual-spacecraft VLBI).